Journal of Nonlinear Optical Physics & Materials
Vol. 12, No. 4 (2003) 1–22

World Scientific
www.worldscientific.com

METAL-DIELECTRIC COMPOSITE FILTERS WITH CONTROLLED SPECTRAL WINDOWS OF TRANSPARENCY

DENTCHO A. GENOV, ANDREY K. SARYCHEV and VLADIMIR M. SHALAEV
School of Electrical and Computer Engineering,
Purdue University, West Lafayette, Indiana 47907-1285, USA

Received 25 June 2003

In this report we show the possibility of broadband low-pass filters with windows of transparency in pre-set spectral ranges. Those filters are based on the unique optical properties of metal-dielectric composites near the percolation threshold. In such composites, metal clusters of different sizes and shapes have different plasmon resonances and resonate nearly independently at different wavelengths. All together, the resonant plasmon modes cover a very broad spectral range. Applying the effect of spectrally selective photo-modification, we develop a procedure that creates mid-infrared windows of transparency within the broadband filters. We also investigate the possibilities of making low-pass filters composed of spheroids and conductive sticks with certain distributions of aspect ratios.

Keywords: Photomodification; absorbtion; semi-continuous films.

1. Introduction

The optical properties of metal-dielectric composites are known to be unique with manifestation of effects that are absent in the constituent bulk metal and dielectric components.[1] One particular example of these properties is the anomalous absorption and extinction that occur in the visible and infrared spectral ranges. Such a broad spectral response is only possible at metal concentrations close to the percolation threshold where, according to the percolation theory,[2] clusters with arbitrary sizes and shapes are present in the composite. For lower metal concentrations the interaction of the composite with an incident electromagnetic field is weaker and the composite becomes semi-transparent for frequencies that are away from the single particle plasmon resonance.

The local field peculiarities, present in metal-dielectric films, were recently successfully described by scale renormalization theory based on the assumption of plasmon localization.[3,4] It was theoretically shown that disorder-induced localization represents a special case of Anderson localization where localized as well as delocalized modes are present in the system.[3,5,6] The delocalized modes determine the global transmission properties of the percolating composites while the localized plasmons play a major role in the local field statistics. The effects of plasmon

localization and giant local field enhancement are also confirmed in experimental studies showing good correspondence with the theoretical predictions.[7,8]

The excitation of plasmon resonances in metal-dielectric films is easily understood by simple analogy where we view the metal clusters as conductive elements with inductances L and the dielectric host as a capacitor C. If the incident beam has a frequency ω_0 which is close to the $L-C$ resonance $\omega_r = (LC)^{-1}$, this will lead to strong absorption and scattering at the same frequency. Recalling that the inductance of a system of interconnected wires (equivalent to the metal clusters present in the composite) depends on the system size and shape, we can expect that at the percolation threshold, where metal clusters of any size and shape are present, the film will effectively support plasmon oscillations in a very broad frequency range. The local electric and magnetic fields are much enhanced compared to the incident field because the local nanoantennas associated with the plasmon modes excited in the composite have very high quality factors Q.[3] The fractal, scale-invariant geometry of the percolation composite localizes the plasmon modes in small spatial regions "hot" spots. This concentration of energy, manifested as local field enhancement, plays an important role in various nonlinear processes such as surface enhanced Raman scattering (SERS), Kerr effect, anomalous absorption, etc.[1]

In this work we investigate the absorption properties of metal-dielectric nanocomposites in the visible and infrared spectral range. We show that very effective obscurants can be made from dielectric microparticles coated with near-2D semicontinuous metal films. One can utilize any lightweight dielectric material that has a low dielectric constant as a host, and noble metals such as gold, silver or copper for the metal component. By inducing local, spectrally-selective photomodification in the composite layer it is possible to create transparency windows in nearly any desired spectral range.[9] Thus, aerosol particles coated with such film will cause efficient light extinction for all wavelengths in the visible and infrared except for the photomodification-induced transparency windows.

The rest of this paper is organized as follows. In Sec. 2 we give a short review of the basic physics that govern the optical response of random films. We also emphasize the analytical and numerical approaches used to determine the respective optical quantities. In Sec. 3, we introduce a new numerical method which is used throughout the paper to determine the respective optical properties of metal-dielectric composite aerosols in the visible and the infrared parts of the spectrum. Requirements for the creation of transparency windows and optimization of their characteristics are described here in detail. In Sec. 4 we concentrate on a different approach, where spheroids with different shapes are studied in terms of their extinction properties. Specific shapes of the aspect ratio distribution functions for creating transparency windows are proposed. Non-quasistatic effects such as the skin effect are investigated for long conducting sticks. Finally, in Sec. 5 we discuss the results and draw some conclusions.

2. Small Particles — Overview

In this section we study small particles that are coated with a metal-dielectric film. The metal-dielectric film is produced, for example, by thermal evaporation or sputtering of metal onto an insulating substrate which, in particular, can be a dielectric, micro-sized aerosol particle. In the growing process, first small metallic grains are formed on the substrate. A typical size a of a metal grain is 5 nm to 20 nm. As the film grows, the metal filling factor increases and coalescence occurs, so that irregularly shaped self-similar (fractal) clusters of particles are formed on the substrate. The sizes of the fractal structures diverge in the vicinity of the percolation threshold, where an "infinite" cluster is eventually formed,[10,11] representing a continuous conducting path between the ends of a sample. At the percolation threshold a structural insulator-metal transition occurs in the system.

The electrical properties of a composite that is homogenous on the length scale of interest can be described by effective quantities such as effective conductivity σ_e or effective dielectric permittivity ϵ_e. Historically two different mean-field approximations were used to estimate these quantities. The first is the Maxwell-Garnett (MGT) theory where particles with dielectric constant ϵ_2 are imbedded in a host dielectric material with constant ϵ_1.[12] The effective dielectric constant ϵ_e is calculated from the relation:

$$\frac{\epsilon_1 - \epsilon_e}{\epsilon_1 + \eta(\epsilon_e - \epsilon_1)} + p\frac{\epsilon_2 - \epsilon_1}{\epsilon_1 + \eta(\epsilon_2 - \epsilon_1)} = 0, \tag{1}$$

where p is the volume fraction and η is the depolatization factor of the inclusions ($\eta = \frac{1}{3}$ for spheres). This equation does not take into account interactions between the inclusions and thus is valid only for small concentrations p. It is also non-symmetric under exchange between ϵ_2 and ϵ_1. The second approach, which is extensively used in the theory of disordered systems, is Bruggeman effective-medium theory (EMT)[13]:

$$p\frac{\epsilon_2 - \epsilon_e}{\epsilon_e + \eta(\epsilon_2 - \epsilon_e)} + (1-p)\frac{\epsilon_1 - \epsilon_e}{\epsilon_e + \eta(\epsilon_1 - \epsilon_e)} = 0, \tag{2}$$

where the two components participate in the equation on equal basis and have concentrations p and $1-p$ respectively. This approximation is believed to better describe the binary mixtures at the percolation threshold, but it also does not account for the interactions between the inclusions.

We can achieve much better estimates of the effective dielectric constant at the percolation threshold by using the scaling theory. As follows from the optical theorem applied to metal-dielectric composites, the effective quantity ϵ_e can, in general, be represented as[10,14]:

$$\epsilon_e = p\epsilon_m\frac{\langle|\mathbf{E}(\mathbf{r},p)|^2\rangle_m}{|\mathbf{E}_0|^2} + (1-p)\epsilon_d\frac{\langle|\mathbf{E}(\mathbf{r},p)|^2\rangle_d}{|\mathbf{E}_0|^2}, \tag{3}$$

where the angular brackets, $\langle\cdots\rangle_d$ and $\langle\cdots\rangle_m$, denote the spatial averaging over the dielectric $\epsilon_d = \epsilon_1$ and metal $\epsilon_m = \epsilon_2$ sides, while $\mathbf{E}_0$ is the incident electric field. The field factors in Eq. (3) represent the average enhancement of the local fields in the metallic and dielectric parts of the composite. As we will show below, because of the high local fields $|\mathbf{E}(\mathbf{r})| \gg |\mathbf{E}_0|$, resulting from plasmon excitation, those factors can be very large for both components of the composite. Accordingly this leads to strong absorption in the broad frequency range.

The dielectric constant of a metal is approximated by the Drude formula $\epsilon_m = \epsilon_b - (\omega_p/\omega)^2/(1 + i\omega_\tau/\omega)$, where ϵ_b is the interband contribution, ω_p is the plasma frequency, and $\omega_\tau = \Gamma$ is the plasmon relaxation rate ($\omega_\tau \ll \omega_p$). In the high-frequency range considered here, the real part ϵ'_m of the metal dielectric function ϵ_m is much larger (in modulus) than the imaginary part ϵ''_m, i.e. the loss parameter κ is small, $\kappa = \epsilon''_m/|\epsilon'_m| \cong \omega_\tau/\omega \ll 1$. We note that ϵ'_m is negative for frequencies ω less than the renormalized plasma frequency, $\tilde{\omega}_p = \omega_p/\sqrt{\epsilon_b}$.

Since ϵ'_m is negative, metal particles can be thought of as inductor-resistor, $L-R$, elements (with R being responsible for losses), whereas dielectric gaps between the particles can be treated as capacitive (C) elements. Then, the condition $\epsilon'_m = -\epsilon_d$ means that the conductivities of the $L-R$ and C elements are equal in magnitude and opposite in sign, i.e. there is a resonance in the equivalent $L-R-C$ circuit corresponding to *individual* particles. For $\epsilon'_m = -\epsilon_d$ the local field in resonating particles is enhanced by the resonance quality-factor Q_0 (which is the inverse of the loss-factor, $Q_0 = \kappa^{-1}$) so that the field enhancement in this case is estimated roughly by κ^{-1}.

For metal concentrations close to the percolation threshold $p = p_c$ a more careful analysis, taking into account the interaction of particles in fractal clusters formed at the percolation threshold yields for the average enhancement of the local field intensity in the dielectric component the following expression[1,3,4]:

$$G_d = \frac{\langle|\mathbf{E}(\mathbf{r}, p_c)|^2\rangle_d}{|\mathbf{E}_0|^2} \sim (|\epsilon'_m|/\epsilon''_m)|\epsilon_m/\epsilon_d|^{\nu/(t+s)}. \tag{4}$$

where the indices t and s are the percolation critical exponents for the conductivity and dielectric constants, respectively, and ν is the critical index for the percolation correlation length, $\xi \sim |p - p_c|^{-\nu}$. For 2D systems, $t \approx \nu \approx s \approx 4/3$ and for 3D systems, the indices are given by $\nu \approx 0.89$, $t \approx 2.05$, and $s \approx 0.76$.[10] In the visible and infrared, the metal dielectric constant is much larger compared to the dielectric, $|\epsilon_m| \gg |\epsilon_d|$. Also, as follows from the Drude formula, for frequencies exceeding the plasmon relaxation rate, i.e. for $\omega \gg \Gamma$ ($\Gamma \equiv \omega_\tau$), we have $|\epsilon'_m| \gg \epsilon''_m$. Thus, according to Eq. (4), the field enhancement G_d (and thus absorption) in the dielectric component can be very large.

Similarly, the average field enhancement in the metallic component of a composite, G_m, can be estimated as[1,3,4]:

$$G_m = \frac{\langle|\mathbf{E}(\mathbf{r}, p_c)|^2\rangle_m}{|\mathbf{E}_0|^2} \sim (|\epsilon'_m|/\epsilon''_m)|\epsilon_d/\epsilon_m|^{t/(t+s)}. \tag{5}$$

where, similar to the enhancement in the dielectric component Eq. (4), we can obtain a large G_m if $\omega \gg \Gamma$ when $|\epsilon'_m| \gg \epsilon''_m$.

Using the effective dielectric constant of the film ϵ_e given by Eq. (3), we can now estimate the absorption properties of aerosol particles dispersed in the air. Here we concentrate on two types of particles in the quasistatic limit. First, the aerosols are viewed as spherical entities with radius r composed of a metal-dielectric mixture (ϵ_e) at the percolation threshold. Second, the aerosol particles are again spherical but are now comprised by core with inner radius r_i and dielectric constant ϵ_i and an outer shell of composite material with thickness $r - r_i$ and dielectric constant ϵ_e. The general formula for the polarizability of the described particles is given in the quasistatic limit as[13]:

$$\alpha = 4\pi r^3 \frac{(\epsilon_e - \epsilon_2)(\epsilon_i + 2\epsilon_e) + f(\epsilon_i - \epsilon_e)(\epsilon_2 + 2\epsilon_e)}{(\epsilon_e + 2\epsilon_2)(\epsilon_i + 2\epsilon_e) + f(2\epsilon_e - 2\epsilon_2)(\epsilon_i - \epsilon_e)} \tag{6}$$

where ϵ_2 is the dielectric constant of the medium in which the aerosol is dispersed (for air $\epsilon_2 = 1$) and $f = (r_i/r)^3$ is the fraction of the total particle volume occupied by the core. It is evident that for $f \to 0$ we recover the case where the aerosol is a 3D metal-dielectric composite.

Using the polarizability from Eq. (6) we can easily calculate the absorption cross section $S_a = \frac{2\pi}{\lambda} \mathrm{Im}(\alpha)$,[13] where λ is the incident beam wavelength. In Fig. 1 we show the specific (per unit volume) absorption cross section $Q_a = S_a/V_p = \frac{6\pi}{\lambda} \mathrm{Im}(\alpha_0)$, where $\alpha_0 = \alpha/3V_p$ and $V_p = 4\pi r^3/3$ is the geometrical volume of the spherical particle. In our calculations we assume a core dielectric constant of $\epsilon_i = 2.2$ (glass) and a silver metal-dielectric film with filing factor $p = p_c$. Assuming a thin film the effective quantity ϵ_e is estimated from an exact solution in the quasistatic limit ($a \ll \lambda$), $\epsilon_e = \sqrt{\epsilon_e \epsilon_i}$ (see Ref. 15), but can also be qualitatively determined from Eqs. (3)–(5).

From Fig. 1 it is evident that introduction of metal dielectric composite as a coating or as a bulk constitutive leads to a strong increase of the absorption in the

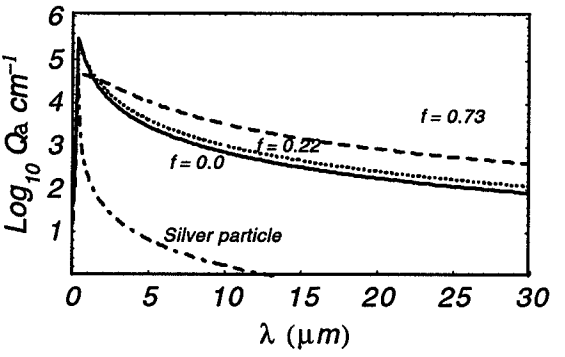

Fig. 1. Absorption cross-section of 100 nm aerosol particles coated with silver metal dielectric film of different thicknesses.

infrared part of the spectrum. For all thicknesses of the coating we obtain absorption that is by a few orders of magnitude higher then what is expected from a bulk silver particle with the same radius. This effect as explained in the analysis above is due to the unique properties of the metal dielectric films in the visible and infrared spectral ranges.

3. Photomodification-Induced Spectral Windows

3.1. *Numerical approach*

Illumination of semicontinuous films with a laser beam that has an intensity higher than some threshold value was shown to induce local spatial modification due to melting and evaporation of the metal grains or due to sinthering process.[16] In our experiments, significant changes to the local field topology were recorded after irradiation of a silver film with ten nanosecond laser pulses at $\lambda_i = 633$ nm and an energy density of 4.5 mJ/cm^2. The experimental results are qualitatively described by simulating the burning process simply as a removal of all metal grains that experience local field intensities (currents) higher than some threshold value. In our calculations, an approximate procedure, real space renormalization group (RSRG) method was used. This method gives good estimates for the highest local field but fails in the description of the exact field distribution. In the discussion below we will show that in order to maintain the photomodification process in an adiabatic mode, the exact scaling for the local intensity has to be known. To determine the local field distribution we develop a new numerical procedure that allows the calculation of all relevant local parameters in random metal-dielectric films in the quasistatic approximation. By applying this new model, we calculate the effective dielectric constant of the film before and after the photomodification. We show that illumination of the sample with a laser beam tuned at a particular wavelength leads to photomodification of the film and a substantial decrease of the absorption in a spectral window centered at the illuminating wavelength.

The numerical modeling of semicontinuous films is a difficult computational problem. At the percolation threshold, an infinite cluster spreads across the whole sample leading to a size dependence of the effective quantities if the sample size L is smaller than the relevant resonance length $l_r(\lambda) \sim a(\lambda/\lambda_p')^{2\nu/(t+s)}$, where λ is the wavelength of interest and $\lambda_p' = \lambda_p\sqrt{\epsilon_b}$ is the renormalized plasma wavelength. Our estimates show that for $\lambda \geq 10\ \mu$m, one has to work with samples that have sizes $L \geq 120a$. Such sizes cannot be calculated with commonly-used numerical procedures such as Gaussian or LU eliminations and new approaches have to be implemented. Below we describe a new direct numerical method, which we refer to as block elimination (BE). The BE method allows calculations of effective parameters such as the conductivity and dielectric permittivity and, most importantly, the local field distribution in inhomogeneous media.

We consider the problem of a local field distribution in nanoscale metal-dielectric films near and away from the percolation threshold in the case when

the wavelength λ of an incident light is much larger than the metal grain size a. Under this condition we can introduce a local potential $\varphi(\mathbf{r})$ and a local current $\mathbf{j}(\mathbf{r}) = \sigma(\mathbf{r}) \cdot (-\nabla\varphi(\mathbf{r}) + \mathbf{E}_0)$, where $\mathbf{E}_0$ is the applied field and $\sigma(\mathbf{r})$ is the local conductivity. In the considered quasistatic case, the problem of the potential distribution is reduced to the solution of the current conservation law $\nabla \cdot \mathbf{j}(\mathbf{r}) = 0$, which leads to the Laplace equation $\nabla \cdot [\sigma(\mathbf{r}) \cdot (-\nabla\varphi(\mathbf{r}) + \mathbf{E}_0)] = 0$ for determining the potentials. Now we discretize the above relation on a square lattice so that the film which is a binary composite of metal and dielectric particles can be represented through metal and dielectric bonds connecting the lattice sites. Under such discretization the current conservation for lattice site i acquires the following form

$$\sum_j \sigma_{ij}(\varphi_i - \varphi_j + E_{ij}) = 0\,, \tag{7}$$

where φ_i is the field potential of site i. The summation is over the nearest (to i) neighbor sites j; $\sigma_{ij} = \sigma_{ji}$ are the conductivities of bonds that connect neighbor sites i and j and E_{ij} are the electromotive forces. The electromotive forces E_{ij} are defined so that $E_{ij} = aE_0$, for the bond leaving site i in the "$+y$" direction, and $E_{ij} = -aE_0$, for the bond in the "$-y$" direction; E_{ij} is zero for the "x" bonds. Note that $E_{ij} = -E_{ji}$.

Numerical solution to the Kirchhoff's equations (7) in the case of large lattice sizes encounter immense difficulties and require very large computational memory storage and high operational speed. A full set of the Kirchhoff equations for square lattice with size L is comprised of L^2 separate equations. This system of equations can be written in the matrix form

$$\hat{\mathbf{H}} \cdot \mathbf{\Phi} = \mathbf{F}\,, \tag{8}$$

where $\hat{\mathbf{H}}$ is a symmetric $L^2 \times L^2$ matrix that depends on the structure and composition of the lattice, $\mathbf{\Phi} = \{\varphi_i\}$ and $\mathbf{F} = \{-\sum_j \sigma_{ij}E_{ij}\}$ are vectors of size L^2 which represent the potentials and applied field in each site and bond. In the literature, the matrix $\hat{\mathbf{H}}$ is called the Kirchhoff Hamiltonian (KH) and it is shown to be similar to the Hamiltonian for the Anderson transition problem in quantum mechanics.[3,4,7] The Kirchhoff Hamiltonian is a sparse random matrix with diagonal elements $H_{ii} = \sum_j \sigma_{ij}$ (where the summation is over all bond conductivities σ_{ij} that connect the ith site with its neighbors) and nonzero off-diagonal elements $H_{ij} = -\sigma_{ij}$.

In principle, Eq. (8) can be solved directly by applying the standard Gaussian elimination technique to the matrix $\hat{\mathbf{H}}$.[17] This procedure has a computational time proportional to $\sim L^6$ and requires a memory space in the order of L^4. Simple estimations show that the direct Gaussian elimination cannot be applied for large lattice sizes ($L > 40$) because of the memory restrictions and long computational times for all contemporary personal computers. Fortunately, the KH matrix $\hat{\mathbf{H}}$ has a simple symmetrical structure that allows implementation of the block elimination procedure that can significantly reduce the operational time and memory requirements.

In calculations we can apply the periodic boundary conditions for the "x" and "y" directions; alternatively, we can also impose parallel or "L"-electrode type boundaries. In the case of the periodic boundary conditions, we suppose that the sites in the first row of the $L \times L$ lattice are connected to the Lth row, whereas the sites of the first column are connected to the last column. Then the Kirchhoff's equations for the first site in the first row, for example, have the following form

$$\sigma_{1,L}(\varphi_1 - \varphi_L) + \sigma_{1,2}(\varphi_1 - \varphi_2) + \sigma_{1,L^2-L+1}(\varphi_1 - \varphi_{L^2-L+1} - aE_0) + \sigma_{1,L+1}(\varphi_1 - \varphi_{L+1} + aE_0) = 0\,, \tag{9}$$

where $\sigma_{1,L}$ is the conductivity of the bond connecting the first and the last sites in the first row. The $\sigma_{1,2}$ conductivity connects the first and second sites in the first row, σ_{1,L^2-L+1} connects the first site of the first row and the first site of the Lth row, $\sigma_{1,L+1}$ connects the first sites of the first and the second rows, and the external field E_0 is applied in the "$+y$" direction. Note that the $\sigma_{1,L}$ and σ_{1,L^2-L+1} connections are due to the periodic boundary conditions in the "x" and "y" directions, respectively.

In Eq. (9) we number the sites of the $L \times L$ lattice "row by row", from 1 (for the first site in the first row) to L^2 (for the last site in the Lth row). Under this labeling the KH matrix $\hat{\mathbf{H}}$ acquires a block-type structure. As an example, for a system with size $L = 5$, the matrix $\hat{\mathbf{H}}$ takes the following block form:

$$\hat{\mathbf{H}} = \begin{pmatrix} h^{(11)} & h^{(12)} & 0 & 0 & h^{(15)} \\ h^{(21)} & h^{(22)} & h^{(23)} & 0 & 0 \\ 0 & h^{(32)} & h^{(33)} & h^{(34)} & 0 \\ 0 & 0 & h^{(43)} & h^{(44)} & h^{(45)} \\ h^{(51)} & 0 & 0 & h^{(54)} & h^{(55)} \end{pmatrix}, \tag{10}$$

where $h^{(jj)}$ are $L \times L$ matrices with diagonal elements $h_{ii}^{(jj)} = \sum_k \sigma_{i+(j-1)L,k}$ (the summation is over the nearest neighbors of the site $i + (j-1)L$, which are located in the jth row, $1 \le i \le L$), while the diagonal matrices $h^{(kl)} = h^{(lk)} (k \ne l)$ connect the kth row with the lth row and vice versa. The matrices in the right upper and in the left bottom corners of the KH matrix $\hat{\mathbf{H}}$ are due to the periodical boundary conditions: they connect the top and the bottom rows and the first and the last columns. The explicit forms for the matrices $h^{(jj)}$ and $h^{(kl)}$ are given in the Appendix.

For large sizes L, the majority of the block $h^{(ij)}$ are zero matrices and thus Gaussian elimination will be a very inefficient way to solve the system Eq. (8). In fact in a process of elimination of all block elements below $h^{(11)}$ in matrix Eq. (10), the only matrix elements that will change are $h^{(11)}$, $h^{(12)}$, $h^{(22)}$, $h^{(15)}$ and $h^{(55)}$ with two more elements appearing in the second and last rows. Thus to eliminate the first block column of the KH we can instead of $\hat{\mathbf{H}}$, work with the following $3L \times 3L$ block

matrix (recall that in the considered example we choose, for simplicity, $L = 5$):

$$\hat{\mathbf{h}}^{(1)} = \begin{pmatrix} h^{(11)} & h^{(12)} & h^{(15)} \\ h^{(21)} & h^{(22)} & 0 \\ h^{(51)} & 0 & h^{(55)} \end{pmatrix}. \tag{11}$$

Now to eliminate the first block column of matrix $\hat{\mathbf{h}}^{(1)}$ we apply a standard procedure,[19] where by using the diagonal elements of block matrix $h^{(11)}$ as pivots we transform $h^{(11)}$ in a triangle matrix $h^{*(11)}$and simultaneously eliminate $h^{(21)}$ and $h^{(51)}$. The elimination of the first column of $\hat{\mathbf{h}}^{(1)}$ and respectively $\hat{\mathbf{H}}$ thus requires only L^3 simple arithmetical operations compared with L^5 operations needed if we work directly with the whole matrix $\hat{\mathbf{H}}$. After the first step of this block elimination is completed the matrix $\hat{\mathbf{H}}$ has the following form:

$$\hat{\mathbf{H}}^{(1)} = \begin{pmatrix} h^{*(11)} & h^{*(12)} & 0 & 0 & h^{*(15)} \\ 0 & h^{*(22)} & h^{(23)} & 0 & h^{(25)} \\ 0 & h^{(32)} & h^{(33)} & h^{(34)} & 0 \\ 0 & 0 & h^{(43)} & h^{(44)} & h^{(45)} \\ 0 & h^{(52)} & 0 & h^{(54)} & h^{*(55)} \end{pmatrix}, \tag{12}$$

where, by the "$*$" superscript, we denote all blocks that have changed in the elimination process. The two new block elements $h^{(25)}$ and $h^{(52)}$ appeared due to the interactions of the first row with the second and the fifth rows.

As a second step, we apply the above procedure for the minor $\hat{\mathbf{H}}_{11}^{(1)}$ of the matrix $\hat{\mathbf{H}}^{(1)}$ (which now plays the role of $\hat{\mathbf{H}}$), therefore we work again with the $3L \times 3L$ matrix:

$$\hat{\mathbf{h}}^{(2)} = \begin{pmatrix} h^{*(22)} & h^{(23)} & h^{(25)} \\ h^{(32)} & h^{(33)} & 0 \\ h^{(52)} & 0 & h^{*(55)} \end{pmatrix}. \tag{13}$$

Repeating with $\hat{\mathbf{h}}^{(2)}$ all of the operations we performed on $\hat{\mathbf{h}}^{(1)}$, we put $h^{*(22)}$ in the triangle form and eliminate $h^{(32)}$ and $h^{(32)}$. We continue this procedure until the whole matrix $\hat{\mathbf{H}}$ is converted into the triangular form with all elements below the diagonal equal to zero. The backward substitution for a triangular matrix is straightforward, namely we obtain first the site potentials in the Lth row (the fifth row, in our example) and then we calculate the potentials in the $L-1$ row and so on, until the potentials in all rows are obtained. The total number of operations needed is estimated as $\sim L^4$ for the described block elimination (BE) method, which is less than the number L^6 needed for Gaussian or **LU** (for symmetric matrixes) elimination.[17] The BE method has an operational speed on the same order of magnitude as in the transfer-matrix method[18] and the Zekri–Bouamrane–Zekri (ZBZ) method.[19] However, BE allows the calculation of the local fields, as opposed to the Franck–Lobb method, and we believe that it is much easier in numerical coding when compared to the ZBZ method.

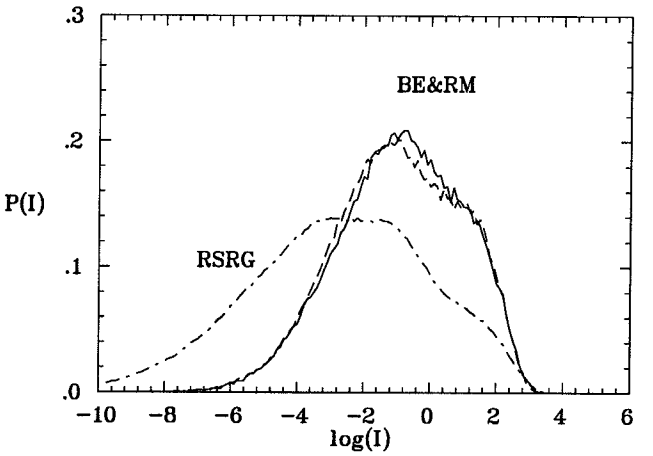

Fig. 2. The local-field distribution $P(I)$ calculated with two exact methods, Relaxation Method (RM) and Block Elimination (BE). Results obtained with the approximate real-space renormalization group (RSRG) are also shown.

We performed various tests to check the accuracy of the BE algorithm described above. First, the sum of the currents in each site was calculated and the average value $\sim 10^{-14}$ was found; this is low enough to claim that the current conservation holds in the method. To further verify the accuracy of the block elimination method, we tested explicitly the field distribution function for the case when the conductivities are positive and real numbers (i.e. the dielectric permittivity is purely imaginary in this case). The local field distribution function (LFDF) we sampled in terms of $\log_{10}(I)$, where $I = (|\mathbf{E} - \mathbf{E}_0|/|\mathbf{E}_0|)^2$ is the local field intensity fluctuations with $|\mathbf{E}_0|^2$ being the intensity of the applied field. If the bond conductivities σ_d and σ_m are positive, we can also apply the relaxation method[20] and compare the results with those obtained with the BE procedure. Such a comparison is presented in Fig. 2, where we can see that both distributions are nearly the same, with only minor deviations due to the differences in the calculation procedures resulting in different round-off errors, and also due to a non-sufficient relaxation times. In the same figure, the local field distribution obtained with the real space renormalization group (RSRG) method is also shown. It exhibits an extended tail toward small values of the intensity I, a fact which is observed for all distributions calculated with this method.

3.2. *Numerical results and scaling theory analysis*

In our analysis of the photomodification process we will first concentrate on the 2D metal-dilectric films at the percolation threshold. The effective dielectric constant ϵ_e of the semicontinuous film is obtained from the local field moments Eq. (3) and used in the calculation of the absorption, transmission and reflection of the thin film. In

all estimates a film thickness of $d = 10$ nm is used. Such a thickness corresponds to the metal particle sizes and is commonly measured for metal concentrations close to the percolation threshold. For a normally incident field, the reflection and transmission amplitudes of a layer of dielectric material with thickness d are given by the equations[21]:

$$r = -x\frac{1 - e^{2iKd}}{1 - x^2 e^{2iKd}}, \tag{14}$$

$$t = \frac{1 - x^2}{1 - x^2 e^{2iKd}} e^{i(K-k)d}, \tag{15}$$

where $x = (K - k)/(K + k)$, $k = 2\pi/\lambda$ is the wave vector of the incident light and $K = k\sqrt{\epsilon_e}$ is the wave vector inside the film. Using the above amplitudes we calculated in Fig. 3 the total absorption $A = 1 - |r|^2 - |t|^2$ and reflection $R = |r|^2$ of a silver film for different metal concentrations. At the percolation threshold the semicontinuous film absorbs in the very broad spectral range with the absolute value of the absorption A and reflection R depending on the film thickness. Our numerical calculations are in perfect agreement with the estimates based on exact result for the effective dielectric constant in the quasistatic limit $\epsilon_e = \sqrt{\epsilon_e \epsilon_2}$.[15] With the slight

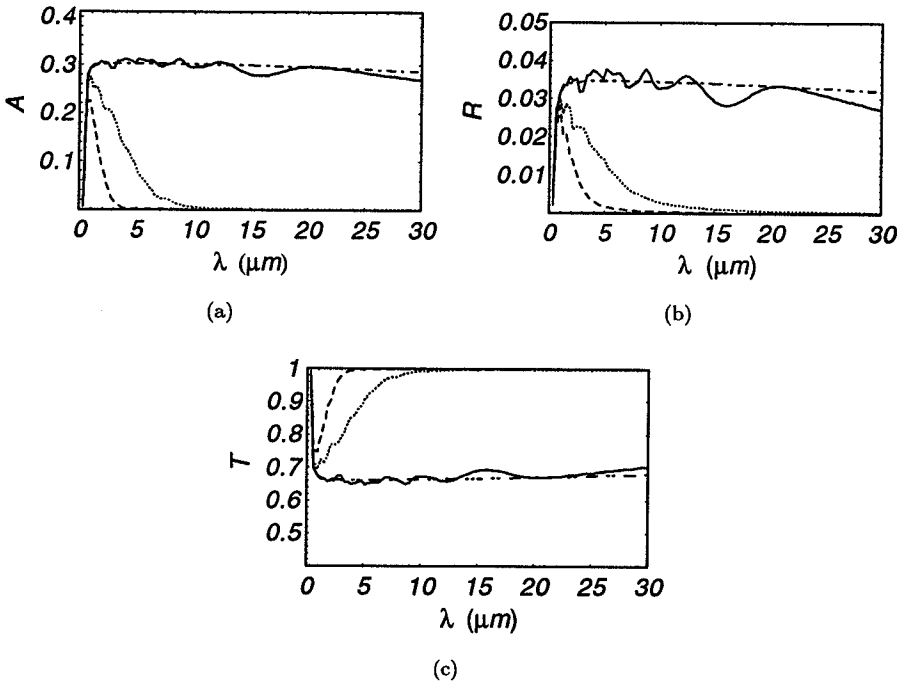

Fig. 3. (a) Absorption, (b) reflection, and (c) transmission calculated for thin film at three different metal filling fractions $p = 0.5$ (solid line), 0.45 (dotted line) and 0.4 (dashed line). The dot-dashed line presents the analytical result at p_c.

decrease of the metal concentration p we see a sharp cutoff in the absorption and reflection of the sample for higher wavelengths. This effect is predicted by the scaling theory where only clusters with sizes large than $l_r(\lambda) \sim a(\lambda/\lambda_p')^{2\nu/(t+s)}$ are viewed as optically active. According to the percolation theory, with the decrease of the metal concentration the correlation length ξ, or the linear size of the largest finite clusters, decreases as $\xi \sim a|p - p_c|^{-\nu}$. Thus there is a cutoff wavelength λ_c such that for all $\lambda > \lambda_c$, the resonance cluster sizes $l_r(\lambda)$ are larger than ξ. It is easy to estimate that in 2D the cutoff wavelength is given with the relation $\lambda_c \sim \lambda_p \sqrt{\epsilon_b} |p - p_c|^{-\nu}$, where $\nu = 4/3$.[10] Based on the above described dependences, metal-dielectric composite can be used as low pass filters in the visible and infrared spectral ranges, with cutoff wavelength set by the control of the metal concentrations.

Random metal-dielectric films with specifically chosen metal concentration may not be the best possible way to create low pass filters. It is very difficult if not impossible to induce a transparency window for a particular wavelength by controlling the metal deposition. Usually the metal-dielectric films are manufactured by continuous deposition of metal grains on a dielectric surface which results in a gradual increase of the maximum cluster sizes. To form a transparency window, a nonlinear procedure of creation or annihilation of large clusters must be used. One such procedure is spatially selective photomodification which was mentioned in the first section of this report. The general idea is to illuminate the semicontinuous film with a high intensity laser beam and thus to destroy only those clusters that resonate at the incident beam wavelength λ_I and have sizes $l \sim l_r(\lambda_I)$. This selective "burning out" is possible because of very strong local currents $\mathbf{j}(\mathbf{r}) = \sigma(\mathbf{r})\mathbf{E}(\mathbf{r})$ that flow through the resonating clusters. To illustrate this phenomenon we have plotted in Fig. 4(a) the local current enhancement factor $|\mathbf{j}(\mathbf{r})|/|\mathbf{j}_0|$ for a silver metal-dielectric film at the percolation threshold. The surface current $\mathbf{j}_0 = \sigma_m \mathbf{E}_0$ is the current in continuously covered metal film ($p = 1$) which is illuminated by an incident field $\mathbf{E}_0$. If the laser intensity I_0 exceeds some photomodification value I_b, this will lead to high heat dissipation in the metal and eventual melting and

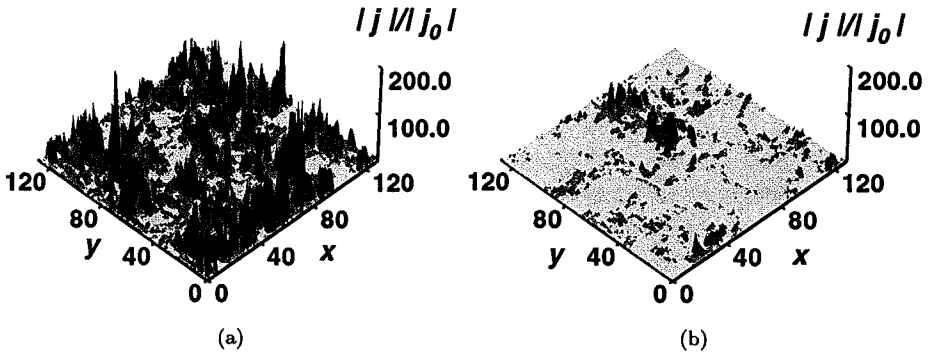

Fig. 4. The local current enhancement in random metal-dielectric films (a) before, and (b) after photomodification induced by an incident beam with wavelength $\lambda_I = 1.5$ μm.

evaporation. This effect destroys the current paths that support resonances and leads to a decrease of the absorption in a spectral range centered around the illuminating wavelength λ_I.

As an example in Fig. 4 we show how the local currents change in the sample after illumination by laser beam with intensity $I_0 = 0.1I_b$. All metal grains that experience local fields higher then I_b are eliminated. Remarkably, during this process only $\sim$0.01% of the metal grains were destroyed which corresponds to a metal concentration of $p = 0.4999$. To see how such a small change in the composition of the film affects the optical properties, in Fig. 5 we show the absorption A and reflection R after adiabatic illumination of the sample at four different pre-set maximum laser intensities $I_{0,\max}$. By the adiabatic illumination we mean that a series of pulses, with gradually increasing intensity was used so that each pulse was able to destroy only a single metal bond of the film where the largest local field exceeded the threshold value I_b. Thus, in each step of our simulation process, the incident field was chosen low enough so that only the maximum local field in a single point of the film exceeded the photomodification value I_b; this bond was removed. Then a

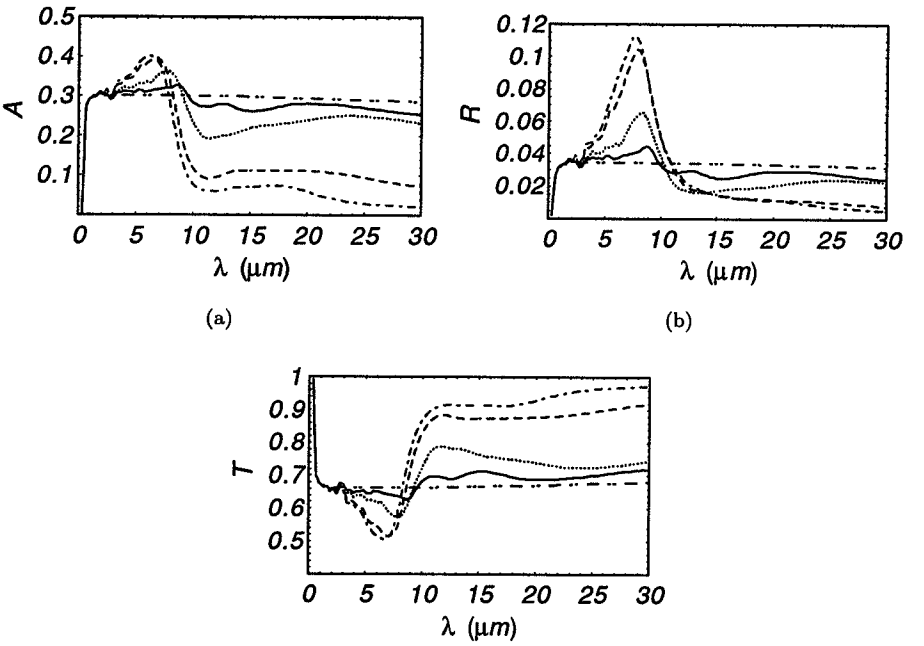

Fig. 5. Photomodification of the (a) absorption, (b) reflection, and (c) transmission spectrum for thin silver film illuminated by a series of light pulses at 10 μm with the maximum intensity given by $I_{0,\max}/I_b = 0.1$ (solid line), 0.2 (dotted line), 0.5 (dashed line) and 0.8 (dot-dashed line). The analytical formulas for A, R, and T for $p = p_c$, without photomodification, are shown as dash double dotted lines.

slightly larger incident field was chosen, which again was sufficient to remove only a single bond where the local intensity exceeded the threshold value. This procedure was continued until what was needed for such an adiabatic photomodification incident field reached a pre-set maximum value $I_{0,\max}$. In all cases of different $I_{0,\max}$, the elimination of a very small number of metal particles leads to a considerable change in the optical properties of the film in the long wavelength range. For example, in the case of the maximum laser intensity equal to half of the "burning" value I_b ($I_{0,\max}/I_b = 0.5$) only $\sim 0.02\%$ of the metal bonds were actually destroyed. Despite such negligible topological change the optical response has changed dramatically as seen in Fig. 5. To explain this effect we use the scaling theory. If we assume that with the destruction of a single bond in a resonating cluster we completely change the resonance properties of this particular cluster, then the fraction of metal grains we need to eliminate is estimated as $p_r \sim [a/l_r(\lambda_I)]^d \sim (\lambda_p'/\lambda_I)^{2d\nu/(t+s)}$. In the 2D case, $p_r \sim (\lambda_p'/\lambda_I)^2 \ll 1$, where for silver $\lambda_p' = \lambda_p\sqrt{\epsilon_b} \simeq 0.3$ μm.[22] Reviewing Fig. 5 we see that by illuminating the semicontinuous film with a strong laser field we can easily create a window or transparency band for wavelengths close to and above the incident beam wavelength λ_I. Since clusters resonating at wavelengths larger than λ_I are greater in sizes they contain smaller parts (with the size $l_r(\lambda_I)$) that are destroyed by the wavelength λ_I. This explains the fact that by irradiating a sample at λ_I one creates the transparency window at this and larger wavelengths. Interestingly enough the absorption and especially the reflection increases for $\lambda \leq \lambda_I$. This can be understood by the increase in the number of clusters with smaller sizes resulting from breaking up the large-sized clusters that have previously supported resonances for the incident field wavelength λ_I. As already mentioned, an adiabatic increase of the incident beam intensity was used during the photomodification process. As more clusters are optically inactivated, the local fields and currents decrease (see Fig. 4) which requires higher incident fields to keep the process going. To work in the adiabatic regime we need to increase the laser intensity in such a way that the maximum local intensity equals or is slightly higher then the burn out value I_b.

The actual scaling of the incident beam intensity that needs to be maintained is shown in Fig. 6. Two different scaling regions are observed. In both region the adiabatic increase of the incident filed intensity is given by the relationship

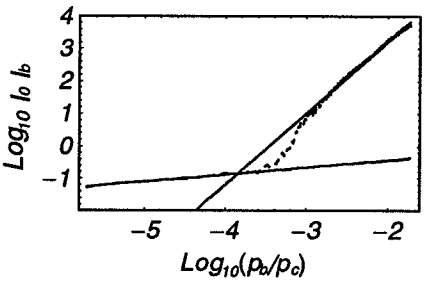

Fig. 6. Required incident field intensity factor as a function of the burned metal fraction. The solid lines represent a power low fitting.

$I_0/I_b \sim (p_b/p_c)^\chi$, where the ratio p_b/p_c is the fraction of the "burned" metal to the total metal deposited. The scaling exponent is estimated as $\chi_1 = 0.21 \pm 0.02$ for the first scaling region and it rises to $\chi_2 = 2.3 \pm 0.2$ for the second.

To explain this type of behavior we again rely on the scaling theory where the maximum local field corresponding to resonating clusters with size l_r is estimated as $E_r/E_0 \sim \kappa^{-1}(l_r/a)$.[1,3,4] For fixed wavelength of illuminations, the local field intensities thus scale as $I_b = I_r \simeq I_0(l_r/a)^2$. To modify this result in terms of the amount of burned metal we use the relation $l_r \simeq \xi \simeq a p_c^\nu |p - p_c|^{-\nu} = a(p_c/p_b)^\nu$, which thus yields $I_0/I_b \sim (p_b/p_c)^\chi$, where $\chi = 2\nu = 8/3$. This result, while slightly higher than the numerically estimated value, gives us a better understanding of the statistics of the burning process. However, it cannot explain the different scaling at the beginning of the photomodification. To understand why at this initial stage we need a very low increase of the incident field intensity for photomodification of the resonating clusters, we have to keep in mind the fact that the sample is illuminated with an electromagnetic field at a particular wavelength λ_I. For this wavelength there are $n_r = p_r L^d \simeq L^d(\lambda_p'/\lambda_I)^{2d\nu/(t+s)}$ resonating clusters with nearly the same quality factors. By eliminating a single bond in each step of the burning process we do not need to increase considerably the laser intensity until all n_r clusters are destroyed. This results in the weaker dependence of I_0 on p_b at the beginning of the photomodification.

Finally, we note that although the adiabatic photomodification allows a better control in creating transparency windows the approach based on a single pulse photomodification can also provide rather good results. In this case one has to carefully choose the intensity of the incident light. To create a larger transparency window one would have to use a laser intensity higher than the threshold value, which would result in the removal of a greater amount of metal particles. As a result, along with the transparency window in the desired spectral range, the absorption outside the transparency window can also become smaller. This explains why one might prefer to use the adiabatic approach for best performance.

4. Absorption Properties of Particles with High Aspect Ratios

4.1. *Quasistatic approximation and spheroidal particles*

In this section we investigate non-interacting spheroidal particles that have a properly selected distribution of the semi-axes. By choosing appropriate distributions of the semi-axes it is possible to create a cutoff or a pre-selected window of transparency in the absorption spectra.

A single ellipsoid is characterized by three depolarization factors η_μ. Only two of these factors are independent with the third given by the relation $\eta_3 = 1 - (\eta_1 + \eta_2)$. In the quasistatic limit the absorption cross-section of the ellipsoid is $S_a = \frac{2\pi}{3\lambda} \sum_\mu \mathrm{Im}(\alpha_\mu)$, where for the polarizabilities α_μ we have[13]:

$$\alpha_\mu = 4\pi abc \frac{\epsilon_m/\epsilon_d - 1}{3 + 3\eta_\mu(\epsilon_m/\epsilon_d - 1)}, \tag{16}$$

and a, b, c and ϵ_m are the three semi-axes and the dielectric constant of the ellipsoid, with $\epsilon_d = 1$ being the dielectric constant of the air. A special case of ellipsoids are the spheroids, which have two axes of equal length. In this case only one of the depolarization factors is independent. For *prolate* (cigar-shaped) spheroids, which have $b = c$ and *eccentricity* e the depolarization factor is given as:

$$\eta_1 = \eta = \frac{1-e^2}{e^2}\left(-1 + \frac{1}{2e}\ln\left(\frac{1+e}{1-e}\right)\right), \tag{17}$$

where $e^2 = 1-(b/a)^2$. The other two factors are equal and are given by the relation $\eta_2 = \eta_3 = (1-\eta)/2$. For *oblate* spheroid (pancake-shaped) with equal axes $a = b$ and *eccentricity* $e^2 = 1-(c/a)^2$, the independent depolarization factor is:

$$\eta_1 = \eta = \frac{g(e)}{2e^2}\left(\frac{\pi}{2} - \tan^{-1} g(e)\right) - \frac{g^2(e)}{2}, \tag{18}$$

with the function g calculated from the relationship $g^2(e) = (e^{-2}-1)$. The shape of the oblate spheroid ranges from a disk ($e = 1$) to a sphere ($e = 0$); that of the prolate spheroid ranges from a needle ($e = 1$) to a sphere.

From Eq. (16) it is easy to see that there are two absorption resonances for both prolate and oblate spheroids. If the spheroids are made of metal (gold, silver, etc.) we can use the Drude approximation $\epsilon_m = \epsilon_b - (\omega_p/\omega)^2/(1+i\omega_\tau/\omega)$ to estimate the resonance condition. After some simple algebraic operations and using $\epsilon_b = 1$ we obtain the following formula for the absorption cross-section:

$$S_a = \frac{8\pi^2 abc}{9\lambda}\left(\frac{\omega_\tau\omega/\omega_p^2}{(\eta-(\omega/\omega_p)^2)^2 + (\omega_\tau\omega/\omega_p^2)^2}\right.$$
$$\left. + \frac{2\omega_\tau\omega/\omega_p^2}{((1-\eta)/2+(\omega/\omega_p)^2)^2 + (\omega_\tau\omega/\omega_p^2)^2}\right). \tag{19}$$

Recalling that for good metals $\omega_\tau/\omega_p \ll 1$, we get estimates for the two resonances in the form $(\omega_r/\omega_p)^2 = \eta$ and $(\omega_r/\omega_p)^2 = (1-\eta)/2$. In terms of the resonance wavelengths we have $\lambda_r^l = \lambda_p/\sqrt{\eta}$ and $\lambda_r^t = \lambda_p/\sqrt{(1-\eta)/2}$. Following the approach presented in Sec. 1, we can calculate the specific cross-section $Q_a = S_a/V_p$, where the volume of the ellipsoid is $V_p = 4\pi abc/3$. The results obtained for prolate and oblate spheroids with uniform distribution of aspect ratios $a/b \in (1,(a/b)_m)$ are presented in Fig. 7.

With the increase in the maximum possible aspect ratio, the depolarization factor asymptotically approaches zero which leads to an increase of the cutoff wavelength λ_r^l. The second absorption resonance is at wavelength close to the plasmon resonance $\lambda_r^t \sim \lambda_p$ and cannot be distinguished in the figures. While the extinction properties of spheroids can be stronger when compared to the coated spherical particles (see Fig. 1), very high aspect ratios are required for the spheroids to absorb in the long wavelength range. This requirement is even stronger for oblate spheroids where, as seen from Fig. 7, the aspect ratios that are higher by a factor

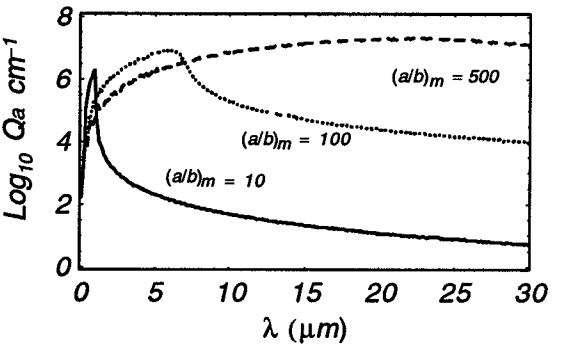

(a)

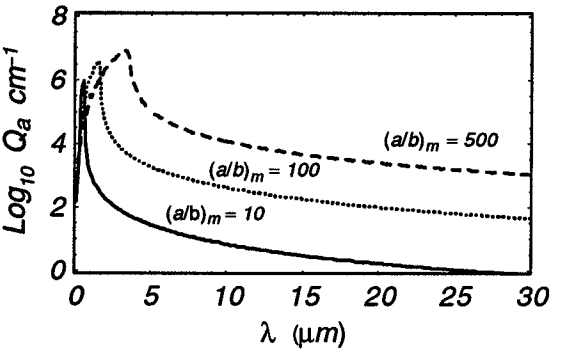

(b)

Fig. 7. Specific absorption for mixtures of (a) prolate and (b) oblate *Ag* spheroids. The aspect ratios vary between one and some maximum value. The maximum aspect ratios $(a/b)_m$ in the particle distributions are included in the figures.

of ten are needed in order to have the same absorption properties as for prolate ellipsoids.

Mixtures of prolate ellipsoids with properly chosen distributions of aspect ratios can be also used to create obscurants that have pre-selected windows of transparency. In Fig. 8 we present the absorption properties of silver ellipsoidal particles with aspect ratios distributed uniformly within two square-like distributions. To create a window of transparency at $\lambda = 10$ μm we excluded particles with aspect ratios in the range from $(a/b)_1 = 150$ to $(a/b)_2 = 350$ (the dashed line in Fig. 8). If $(a/b)_1 = 50$ is used, a decrease of the absorption by two orders of magnitude can be achieved for wavelengths centered around $\lambda = 5$ μm (the solid line in Fig. 8).

While it is possible to create very strong obscurants from mixtures of spheroidal particles that have high aspect ratios, it may be difficult to manufacture such particles. The analysis described above was based on the quasistatic approximation

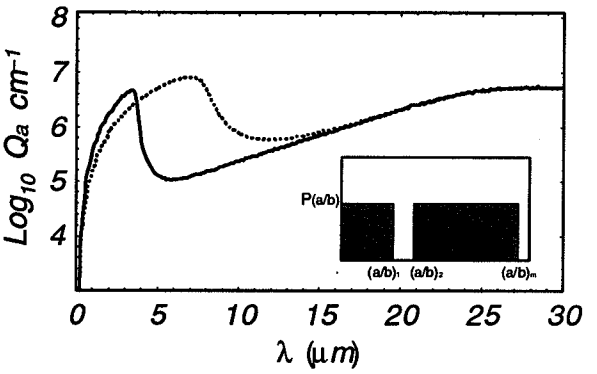

Fig. 8. Windows in the absorption spectrum of mixture of spheroids. The shape of the aspect ratios distribution is shown in the insert.

which demands the maximum sizes of the particles to be smaller than the wavelength. For $\lambda = 10$ μm and aspect ratios of $(a/b)_m = 500$, the thickness of the prolate spheroids must be close to one nanometer. To investigate particles that have bigger sizes and are easier to manufacture, one must account for the skin effect. This is done in the next subsection where conductive sticks with high aspect ratios are investigated.

4.2. *Beyond the quasistatic: conductive sticks*

In order to investigate the effects based on the skin effect, we will concentrate here on systems composed of conductive (metal) sticks with high aspect ratio. The geometric properties of composites with penetrable sticks have been studied both by Monte Carlo simulations[23,24] and analytically.[25,26] It was found that the percolation threshold p_c is universally proportional to the stick aspect ratio $p_c \sim b/a$, where b is the radius of the stick and $2a$ is its length. It was also found that such dependence cannot be explain by the EMT and MGT theories. The first approximation predicts a percolation threshold that is proportional to the depolarization factor of the inclusions in the direction of its major axis, which for very elongated sticks scales as $p_c \sim (b/a)^2 \ll b/a$. Contrary to the EMT predictions, the MGT gives a higher percolation threshold $p_c \sim \sqrt{b/a} \gg b/a$. To resolve this problem, a new effective medium theory was introduced that gives the correct value for the percolation threshold and extends the treatment of the problem beyond the quasistatic case when strong skin effect is present.[27] For small stick concentrations $p \ll b/a$ and strong skin effect, the effective dielectric constant is given as:

$$\epsilon_e = p\epsilon'_e = p\epsilon_d \frac{(a/b)^2}{\ln(a/b)(\cos(ak\sqrt{\epsilon_d}) - i\epsilon_d(ak)^2/2\ln(a/b))} \tag{20}$$

where $k = 2\pi/\lambda$ is wave vector of the incident wave. From Eq. (20) it follows that the effective dielectric constant of conductive sticks has a resonance behavior in the

case of strong skin effect. The resonance wavelengths are given by the condition $\lambda_n = 4a\sqrt{\epsilon_d}/(2n-1)$, $n = 1, 2, \ldots$, each having a quality factor that depends on the aspect ratios, $Q_n \sim (a/b)/((2n-1)\ln(a/b))$. Using Eq. (20) we can calculate the specific extinction cross section Q_a which in this case is given by the relation $Q_a = \frac{4\pi}{\lambda}\,\mathrm{Im}(\sqrt{\epsilon_e'})$.

The results for three different aspect ratios and stick size $a = 2$ μm are shown in Fig. 9. As expected, the quality factor and accordingly the absorption increases with the increase of the aspect ratio a/b. The comparison with Fig. 6 shows that in all cases the skin effect leads to a decrease of the absorption and changes in the resonance properties compared to the quasistatic case.

Similar to the procedure that was implemented in the previous subsection, we can form mixtures of conductive sticks that have pre-selected windows of transparency. To control the absorption properties of mixtures of prolate spheroids we relied on the specific aspect ratio distributions, this however is not the case for the conductive sticks. As we have shown, the resonance wavelengths λ_n depend only on

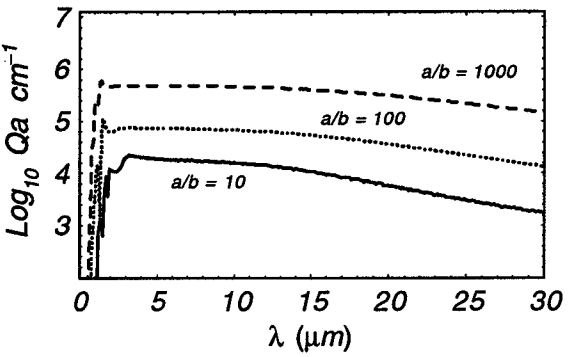

Fig. 9. Specific absorption for conductive sticks with three different aspect ratios.

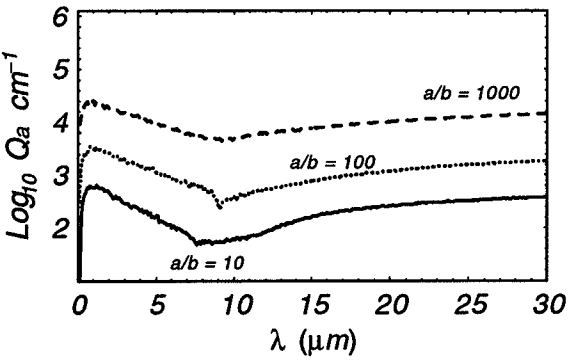

Fig. 10. Transparency windows for three mixtures of conductive sticks, each with varying sizes a and constant aspect ratio a/b.

the length $2a$ of the stick but not on the aspect ratio (although the quality factors do depend on the ratio). Thus, to set a transparency window we can control the distributions over sizes a.

In Fig. 10 we show three different curves where the stick sizes are uniformly distributed in the ranges $a \in (0.1, 1)$ μm and $a \in (10, 100)$ μm. By excluding sticks with lengths in the interval from 1 μm to 10 μm we succeed in forming a transparency window around $\lambda = 10$ μm. With an increase of the aspect ratio the quality factors of the sticks increase which leads to higher absorption throughout the entire spectral range.

5. Conclusions

In this paper we theoretically investigated different ways for creating low-pass broadband filters that have narrow transparency windows in pre-set spectral ranges. We considered dielectric aerosol particles coated with thin, $\sim$10 nm, semicontinuous metal films. Such metal-coated particles can be very efficient obscurants, because of the particularly broad absorption band of the semicontinuous metal films at the percolation threshold. For metal-coated dielectric aerosols we calculate the optical cross-sections and optimize the sizes of the particles, the coating thickness and the concentration of the composite particles needed for efficient obscurity. The long wavelength absorption cross-section of coated aerosol particles is found to surpass by a few orders of magnitude the corresponding values for bulk metal particles with the same sizes. To create a transparency window in the mid-infrared, we employ the local photomodification effect. A new, exact and very efficient numerical model called Block Elimination (BE) was developed. This model allows calculations of the local field properties of very large samples $L \geq 200$, thus for the first time making it possible to study the process of photomodiffication without any initial assumptions or simplifications. Using this new numerical model we studied thoroughly the photoburning of spectral dips in the extinction spectrum of composite aerosols. It was found that very small topological changes lead to dramatic effects in the absorption properties of semicontinuous films. Using adiabatic or instantaneous photoburning, we can create different windows of transparency near pre-set wavelength, for example, at $\lambda = 10$ μm. By controlling the total amount of metal grains removed (by photoburning) we can control the depth of the transparency windows and their width. The scaling of the incident laser intensity for achieving the adiabatic photomodification was determined.

In this report we also present alternative approaches for creating efficient obscurants in the visible and infrared. For this we consider an ensemble of small (less than the wavelength) metal spheroids with different aspect ratios. By choosing proper mixtures of spheroids with aspect ratios within a certain distribution, we achieve strong light extinction in a broad spectral interval. The cutoff wavelengths of the absorption spectrum correspond to the edges of the distribution. By excluding particles with specific aspect ratios we succeeded in forming transparency windows

in the absorption spectrum. In the center of the window the absorption can be lower than the rest of the spectrum by a few orders of magnitude. Compared to the case of coated particles, much higher absorption cross-sections can be achieved by using spheroids in the quasistatic range. For larger particles, conductive sticks are used where the skin effect leads to a new type of phenomena, and the absorption is decreased. The resonances of metal sticks depend on the largest size but not on the aspect ratio. Using sticks with different size distributions it is possible to create obscurants with pre-set windows of transparency, which are similar to the case of spheroids.

References

1. V. M. Shalaev, *Nonlinear Optics of Random Media: Fractal Composites and Metal-Dielectric Films* (Springer, STMP 158, Heidelberg, 2000); A. K. Sarychev and V. M. Shalaev, *Electrodynamics of Composite Materials* (World Scientific, Singapore, 2003).
2. A. Bunde and S. Havlin, *Fractals and Disordered Systems* (Springer Verlag, Heidelberg, 1991).
3. A. K. Sarychev, V. A. Shubin and V. M. Shalaev, *Phys. Rev. B* **60**, 16389 (1999).
4. A. K. Sarychev and V. M. Shalaev, *Phys. Rept.* **335**, 275 (2000).
5. M. I. Stockman, S. V. Faleev and D. J. Bergman, *Phys. Rev. Lett.* **87**, 167401 (2001).
6. D. A. Genov, A. K. Sarychev and V. M. Shalaev, *Phys. Rev. E* **67**, 566 (2003).
7. S. Gresillon, L. Aigouy, A. C. Boccara, J. C. Rivoal, X. Quelin, C. Desmarest, P. Gadenne, V. A. Shubin, A. K. Sarychev and V. M. Shalaev, *Phys. Rev. Lett.* **82**, 4520 (1999).
8. K. Seal, M. A. Nelson, Z. C. Ying, D. A. Genov, A. K. Sarychev and V. M. Shalaev, *Phys. Rev. B* **67**, 035318 (2003).
9. S. Ducourtieux *et al.*, *Phys. Rev. B* **64**, 165403 (2001).
10. D. J. Bergman and D. Stroud, *Physical Properties of Macroscopically Inhomogeneous Media*, in *Solid State Physics*, Vol. 46 (Academic Press, Inc., 1992) p. 147.
11. D. Stauffer and A. Aharony, *Introduction to Percolation Theory*, 2nd edn. (Taylor and Francis, Philadelphia, 1991).
12. D. A. G. Bruggeman, *Ann. Physik* **24**, 636 (1935).
13. C. F. Bohren and D. R. Huffman, *Absorption and Scattering of Light by Small Particles* (John Wiley & Sons, New York, 1998).
14. M. Gadenne, V. Podolskiy, P. Gadenne, P. Sheng and V. M. Shalaev, *Europhys. Lett.* **53**, 364 (2001).
15. A. M. Dykhne, *Zh. Eksp. Teor. Fiz.* **59**, 110 (1970).
16. S. Ducourtieux, V. A. Podolskiy, S. Gresillon, S. Buil, B. Berini, P. Gadenne, A. C. Boccara, J. C. Rivoal, K. Banerjee, V. P. Safonov, Z. C. Ying, A. K. Sarychev and Vladimir M. Shalaev, *Phys. Rev. B* **64**, 165403 (2001).
17. R. Coult *et al.*, *Computational Methods in Linear Algebra* (John Wiley & Sons, New York–Toronto, 1975).
18. B. Derrida and J. Vannimenus, *J. Phys. A: Math. Gen.* **15**, L557 (1982).
19. L. Zekri, R. Bouamrane and N. Zekri, *J. Phys. A: Math. Gen.* **33**, 649 (2000).
20. G. G. Bartrouni, A. Hansen and M. Nelkin, *Phys. Rev. Lett.* **57**, 1336 (1986).
21. Y. Yagil, M. Yosefin, D. J. Bergman, G. Deutscher and P. Gadenne, *Phys. Rev. B* **43**, 11342 (1991).
22. E. D. Palik (ed.), *Handbook of Optical Constants of Solids* (Academic Press, New York, 1985).

23. I. Balberg, N. Binenbaum and N. Wagner, *Phys. Rev. Lett.* **52**, 1465 (1984).
24. I. Balberg, *Phys. Rev. B* **31**, 4053 (1985).
25. C. A. Zuev and A. F. Sidorenco, *Teor. Mat. Fiz.* **62**, 76 (1985).
26. C. A. Zuev and A. F. Sidorenco, *Teor. Mat. Fiz.* **62**, 253 (1985).
27. A. N. Lagarkov and A. K. Sarychev, *Phys. Rev. B* **53**, 6318 (1996).